

QNN Framework based Multiclass Classification for Downlink NOMA Detectors

Hye Yeong Lee, Man Hee Lee, and Soo Young Shin

Abstract—Quantum neural networks (QNNs) have attracted significant attention recently, primarily because of their potential to address complex problems deemed difficult for traditional computational methods. This study explores the viability of QNN in handling multiclass classification tasks in downlink non-orthogonal multiple access (NOMA) frameworks. The investigation includes a design of QNN framework and performance evaluation of a QNN-based NOMA detector, integrating maximum likelihood (ML), successive interference cancellation (SIC), and rotated ML (RML) methods. A QNN framework was configured for all three detectors, and a comparative analysis was conducted in terms of loss, accuracy, and testing across varied signal-to-noise ratio (SNR) levels and power allocation coefficients, considering NOMA-specific characteristics. Furthermore, the computational complexity of each detector was analyzed within the proposed framework.

Index Terms—Detector, non-orthogonal multiple access, quantum neural network.

I. INTRODUCTION

6G is expected to be launched in 2030s [1]. In contrast to previous generations, the upcoming 6G wireless communication systems will be transformative and revolutionize the evolution from “connected everything” to “connected intelligence”. Several crucial enablers have been suggested, such as increased bandwidth, higher data transmission rates, intelligent network optimization, resource allocation, and spectrum management [2]. Future research seeks various artificial intelligence (AI) optimization techniques, including graph neural networks, deep reinforcement learning, semantic communication, federated learning, transfer learning, and quantum neural network (QNN) [3].

QNNs, which leverage the principles of quantum mechanics and machine learning, have attracted significant attention in recent years due to their potential to solve complex problems that are difficult to solve with classical systems. The interest is driven by their potential advantages, including

enhanced trainability, a reduced number of training iterations necessary to achieve similar performance levels, and decreased computational complexity in contrast to classical neural networks [4], [5]. These networks have shown significant potential in fields such as image processing and the design of quantum-enhanced communication systems [6], [7].

In the realm of communication, QNNs promise significant advances, particularly in areas such as multiple-input multiple-output (MIMO) systems, channel estimation, and resource allocation, where classical methods have encountered significant scalability and performance limitations. These innovative capabilities position QNNs as a compelling solution for addressing the intricacies of non-orthogonal multiple access (NOMA) systems [8].

NOMA has been recognized as a key enabling technology for next-generation wireless communication systems that offers superior spectral efficiency and connectivity by allowing multiple users to share the same frequency and time resources. The latest NOMA transceiver leverages deep learning for improved performance and efficiency [9]. Generally, most of the research has focused on the transmitter as power allocation (PA) and user pairing [10]. In [11], QNN with parallel training (PS-QNN) was presented to optimize PA and transmit precoding in MIMO-NOMA. In [12], QNN was exploited for user pairing allocation in NOMA. In addition, reinforcement learning-inspired QNN (RL-QNN) was presented to improve optimization performance.

To the best of our knowledge, the performance of QNN-based detectors in handling downlink NOMA signals remains underexplored. In this work, we investigate the use of QNNs for multiclass classification in downlink NOMA systems. The contributions of this work are as follows.

- A QNN-based NOMA detector is proposed, encompassing maximum likelihood (ML), successive interference cancellation (SIC), and rotated ML (RML).
- Performance evaluation compares the accuracy and computational complexity of three detectors across varied scenarios.
- Additionally, the introduced QNN-based NOMA detector is evaluated against classical neural networks such as deep neural networks (DNN) focusing on training loss and accuracy metrics.

The remainder of this paper is organized as follows. Section II provides a technical overview of NOMA with two superposition coding (SC) methods and three detectors. Section III outlines the motivation for this study and the QNN structure for the NOMA detector. Section IV presents the

Manuscript received December 15, 2024; revised April 14, 2025; approved for publication by Kim, Joongheon, Guest Editor, June 4, 2025.

This work was supported in part by Institute of Information & communications Technology Planning & Evaluation (IITP) grant funded by the Korea government(MSIT) (No. 2021-0-02120, 50%, Research on Integration of Federated and Transfer learning between 6G base stations exploiting Quantum Neural Networks) and in part by the National Research Foundation of Korea(NRF) funded by the Ministry of Science and ICT(MSIT), Korea Government under Grant (RS-2022-NR070834, 50%)

The authors are with the WENS Lab, Department of IT Convergence Engineering, Kumoh National Institute of Technology, Gumi, Gyeongsangbuk-do 39177, South Korea, email: {lhy413, fordmore, wdragon}@kumoh.ac.kr.

S. Y. Shin and M. H. Lee are the corresponding authors.

Digital Object Identifier: 10.23919/JCN.2025.000045

Creative Commons Attribution-NonCommercial (CC BY-NC).

This is an Open Access article distributed under the terms of Creative Commons Attribution Non-Commercial License (<http://creativecommons.org/licenses/by-nc/3.0>) which permits unrestricted non-commercial use, distribution, and reproduction in any medium, provided that the original work is properly cited.

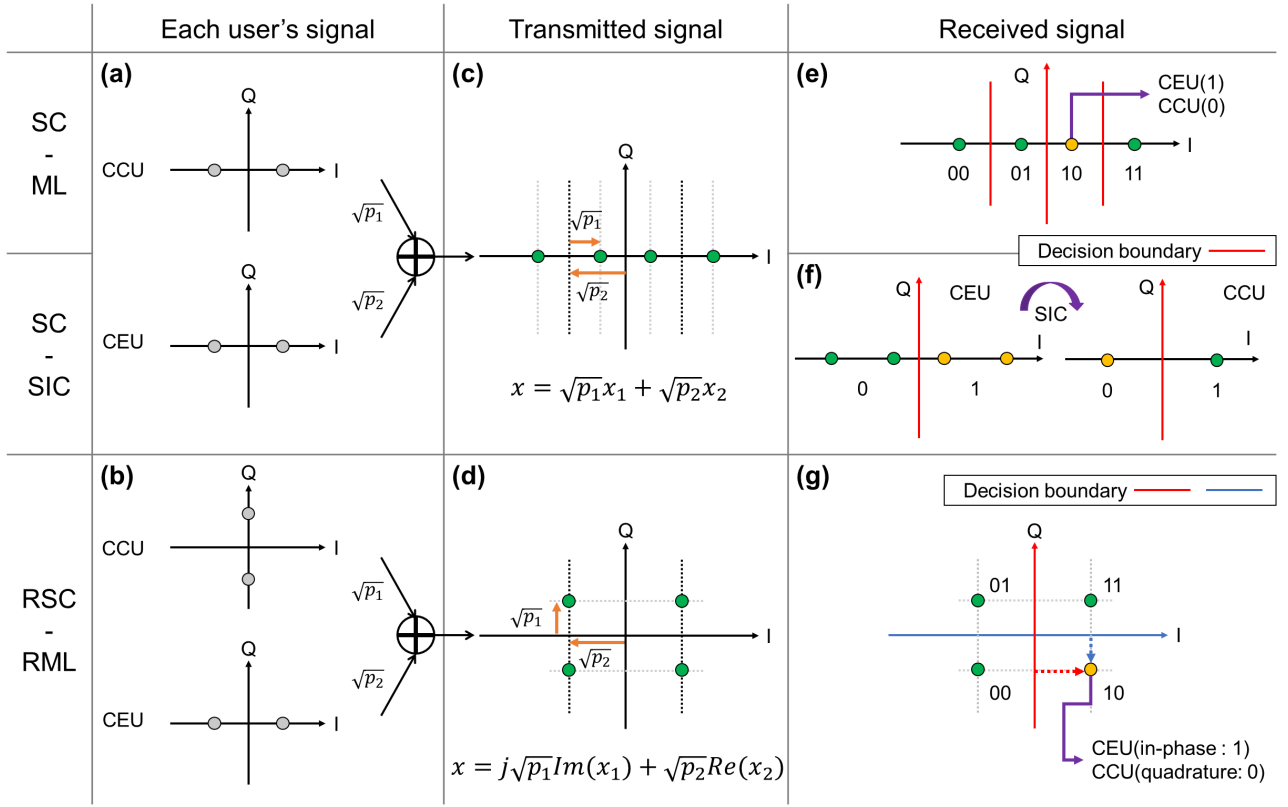


Fig. 1. Various NOMA methods: Each user's signal with (a) superposition coding (SC) and (b) rotated SC (RSC), transmitted signal (c) after SC and (d) after RSC, received signal decoded by (e) maximum likelihood (ML), (f) successive interference cancellation (SIC), and (g) rotation ML (RML).

results and discussion, while Section V concludes with a summary of findings and future research directions.

Notation: The quantum operations discussed in this paper are grounded in [13]. H , R_Z , R_Y , CX , and CZ denote the operation of the Hadamard gate, rotation on the X axis, rotation on Y axis, controlled X gate, and controlled Z gate, respectively. The operator \otimes denotes the Kronecker product. The operators $\text{Re}(\cdot)$ and $\text{Im}(\cdot)$ represent the real and imaginary parts of complex numbers.

II. TECHNICAL OVERVIEW OF NOMA

A. NOMA Principle

In this paper, we assume a downlink NOMA system with two users per pair, i.e., a NOMA pair consists of a cell center user (CCU) and a cell edge user (CEU) to achieve near-far effects. In the transmitter, each user signal is superimposed with distinct power allocations. In downlink NOMA systems, users experiencing small normalized channel gains are typically assigned higher power levels to enhance their signal-to-interference-plus-noise ratio (SINR). Consequently, CEU is allocated higher power levels compared to CCU. In the receiver, several detectors have been proposed to identify individual user signals based on desired performance metrics, including error rate, complexity, known channel/power information, etc.

Fig. 1 compares various NOMA methods that focus on the transmission and received signal constellation points, where both CCU and CEU employ BPSK modulation. In this paper,

we consider two SC methods and three detectors for NOMA system.

1) *Basic superposition coding:* Fig. 1(a) and (c) present the basic SC signal for the transmitted signal. In downlink NOMA, the total power P allocated to all $K = 2$ users with a different power allocation coefficient and then the SC signal x can be expressed as

$$x = \sum_{k=1}^K \sqrt{p_k} s_k, \quad (1)$$

where s_k and p_k denote the transmitted symbol and the transmitted power of the user k . Without loss of generality, P is assumed to be the normalized power as $P = \sum_{k=1}^K p_k = 1$ and $p_k < p_{k+1}$.

2) *Rotation SC:* Fig. 1(b) and (d) present the RSC signal for the transmitted signal in rotated NOMA. The rotated NOMA can construct an SC signal by combining the in-phase component of a user signal with the quadrature component of another user signal. To detect signals without SIC using a single IQ component in the receiver, each user's signal uses a rotated M -ary PSK/QAM symbol with $e^{j\phi_k}$. The SC signal of the rotated NOMA can be expressed as

$$x = \sqrt{p_2} \text{Re}(s_2 e^{j\phi_2}) + j \sqrt{p_1} \text{Im}(s_1 e^{j\phi_1}), \quad (2)$$

where ϕ_k is the rotation angle of M -ary PSK/QAM symbol for the k th user. The optimal rotation angle is assumed to be 90° for BPSK ($M = 2$) and 26.56° for QPSK/QAM ($M = 4$), ensuring an equal error probability

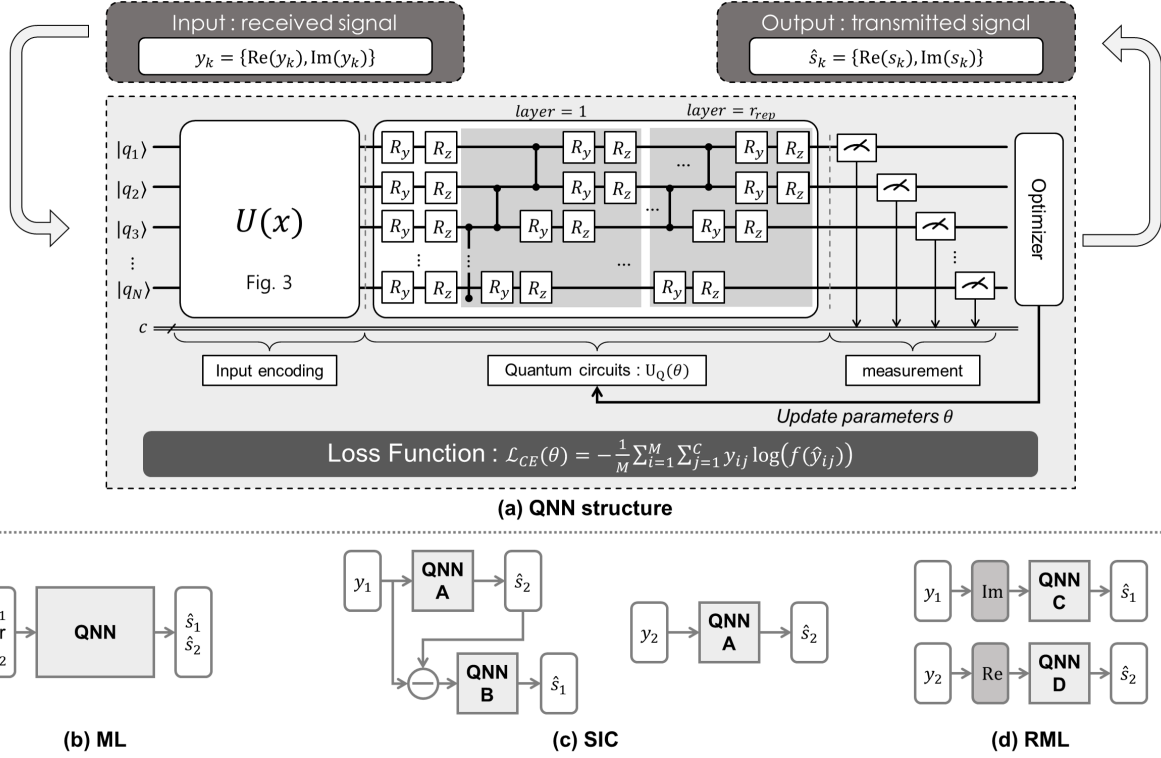


Fig. 2. QNN based NOMA detector (a) QNN structure (b) QNN aided ML detector (c) QNN aided SIC detector (d) QNN aided RML detector.

across adjacent symbols [14], [15]. For example, the CCU signal employs rotated BPSK ($\phi_1 = 90^\circ$), while the CEU applies the conventional BPSK ($\phi_2 = 0^\circ$) to differentiate the IQ constellation, as shown in Fig. 1(b).

B. NOMA Detector

The received signal for k th user can be represented as

$$y_k = h_k \sum_{k=1}^K \sqrt{p_k} x_k + n_k, \quad (3)$$

where h_k and n_k denote the channel and Gaussian noise.

1) *Maximum likelihood*: For the ML detector, each user signal is directly decoded from the received SC signal, and can be given by

$$\begin{aligned} \hat{s}_1 &= \arg \max (|y_1 - \tilde{h}_1 x|^2), \\ \hat{s}_2 &= \arg \max (|y_2 - \tilde{h}_2 x|^2), \end{aligned} \quad (4)$$

where \tilde{h}_k denotes the estimated channel for k th user.

Fig. 1(e) illustrates an example of the ML detector applicable to NOMA signals. The process of estimating the received signal for each user can be carried out to determine the nearest constellation point by employing a uniform decision boundary.

2) *Successive interference cancellation*: To effectively decode each user's signal, the SIC detector is widely utilized for the NOMA system. First, the signal of the user with higher power level (CEU) is decoded by treating other signals as noise. After that, the estimated CEU signal is removed from

the SC signal, and then the CCU signal can be decoded. The sequential user decoding can be expressed as

$$\begin{aligned} \hat{s}_2 &= y_2 / (\tilde{h}_2 \sqrt{p_2}), \\ \hat{s}_1 &= \frac{y_1 - \tilde{h}_1 \sqrt{p_2} \hat{s}_2}{\tilde{h}_1 \sqrt{p_1}}. \end{aligned} \quad (5)$$

Fig. 1(f) shows an example of SIC detector for NOMA signal. When decoding '10' bits, the initial step is to decode the CEU from the received signal by applying the BPSK decision boundary for demodulation. Subsequently, the CCU symbol can be decoded by subtracting the CEU symbol from the received signal by utilizing BPSK decision boundary.

3) *Rotation ML*: In rotated NOMA systems, user signals are decoded similarly to the traditional ML detector. However, in contrast to the ML detector, the rotation ML (RML) method treats either the in-phase or the quadrature component of each user's signal independently, and it can be given by

$$\begin{aligned} \hat{s}_1 &= \arg \max (|\operatorname{Im}(y_1) - h_1 \operatorname{Im}(s_1 e^{j\phi_1})|^2), \\ \hat{s}_2 &= \arg \max (|\operatorname{Re}(y_2) - h_2 \operatorname{Re}(s_2 e^{j\phi_2})|^2). \end{aligned} \quad (6)$$

Fig. 1(g) shows an example of the RML detector for the rotated NOMA signal. From the constellation point for the received signal, the CEU symbol is decoded using the in-phase component via the BPSK decision boundary, while the CCU symbol is decoded from the quadrature component using a rotated BPSK boundary.

III. QNN BASED NOMA DETECTOR

A. QNN based Detector Architecture

Fig. 2 represents the QNN structure for the NOMA detector. In this paper, the input data represent the received signal, and the output data correspond to the estimated signal. The detailed description of the QNN structure is described in the following subsections, as illustrated in Fig. 2(a).

Fig. 2(b), 2(c), and 2(d) illustrate QNN-based NOMA detectors in their roles as ML, SIC, and RML detectors, respectively. In this paper, the NOMA signal operates as the pivotal basis for categorizing various classes of signals within the QNN framework. The number of constellation points of the NOMA signal is given by $\prod_{k=1}^K \mathcal{M}_k$, where \mathcal{M}_k is the modulation order of k th user. Here, we assume that there are $K = 2$ users for a NOMA pair, and the indices assigned to the users represent the indexing CCUs as s_1 and the other CEUs as s_2 .

The architecture of the three NOMA detectors utilizes unique QNN models tailored to their particular inputs and outputs, with the number of qubits N_q configured as follows:

- The ML detector trains the entire NOMA signal for a single QNN framework, as shown in Fig. 2(b), which requires $N_c^{\text{ML}} = \mathcal{M}_1 \mathcal{M}_2$ classes and $\log_2 N_c^{\text{ML}}$ qubits.
- The training framework of the SIC detector is distinct depending on the modulation order specified by the user. When \mathcal{M}_1 is not equal to \mathcal{M}_2 , the SIC detector employs a QNN framework for independent training on CEU and CCU signals, which requires $N_c^{\text{SIC},1} = \mathcal{M}_1$ and $N_c^{\text{SIC},2} = \mathcal{M}_2$ classes and $\sum \log_2 N_c^{\text{SIC},k}$ qubits. Consequently, Fig. 2(c) requires the use of different frameworks for QNN A and B. Otherwise, when \mathcal{M}_1 equals \mathcal{M}_2 , the QNN framework is structured to allow QNN A to be substituted for QNN B in Fig. 2(c). For this scenario, the necessary class and qubit specifications are $N_c^{\text{SIC}} = \mathcal{M}_2$ classes, along with $\log_2 N_c^{\text{SIC}}$ qubits.
- The RML detector independently trains a QNN framework for both CEU and CCU signals, which requires $N_c^{\text{RML},1} = \mathcal{M}_1$ and $N_c^{\text{RML},2} = \mathcal{M}_2$ classes, along with $\sum \log_2 N_c^{\text{RML},k}$ qubits.

B. QNN Structure

A typical QNN architecture for classical data handling, depicted in Fig. 2(a), consists of three stages: encoding the data into quantum states, processing via parameterized quantum circuits (ansatz), and measuring the resultant for classical values to optimize parameters using classical computations. Consequently, the QNN process can be formally represented as follows:

$$U_{QNN} = U_Q(\theta) \circ U_{\text{enc}}(x), \quad (7)$$

where $U_Q(\theta)$ and $U_{\text{enc}}(x)$ indicate the parameterized quantum circuit and the input encoding operations and the input encoding operations, respectively. \circ represents successive operations of distinct quantum operations.

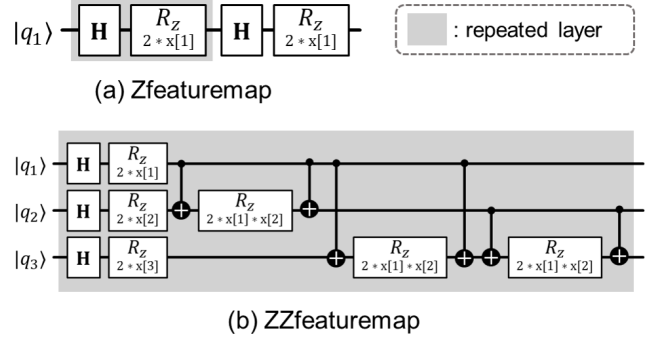


Fig. 3. Design of feature map (a) ZFeatureMap (b) ZZFeatureMap [16].

1) *Input encoding*: Classical NN focuses on how to represent the data numerically, while QNN requires how to represent and input the data efficiently into a quantum system, which is referred to as data encoding [17]. The classical datasets consisting of M samples, each with N features.

Let the received signal $\mathbf{y} = \{y^{(1)}, \dots, y^{(m)}, \dots, y^{(M)}\}$ represent the classical datasets consisting of M samples, each with N features. The received signal constellation point is expressed as complex symbols $y^{(m)} = \text{Re}(y^{(m)}) + j \text{Im}(y^{(m)})$. Here, $\text{Re}(y^{(m)})$ and $\text{Im}(y^{(m)})$ serve as distinct input features and are encoded individually into qubits $|q_1\rangle$ and $|q_2\rangle$, respectively. In this paper, for $N_q > 2$, zero padding is applied to $N_q - 2$ qubits.

Utilizing the encoding operation U_{enc} , classical value $\mathbf{x} \equiv \mathbf{y}$ is transformed into a parameterized quantum state $|\varphi\rangle$, as expressed by

$$\mathbf{x} \xrightarrow{U_{\text{enc}}} |\varphi\rangle. \quad (8)$$

In this paper, we utilize angle encoding to express the fundamental rotation angle of n -qubits as follows.

$$|\varphi\rangle = \bigotimes_{i=1}^N \cos(x_i) |0\rangle + \sin(x_i) |1\rangle. \quad (9)$$

The rotation angle can be represented as a unitary matrix $U(x_j^{(i)})$. A single-qubit rotation around the Y -axis, $U(x_j^{(i)})$ denotes $R_Y(2x_j^{(i)})$ like $|x\rangle = R_Y(2x_j^{(i)})$.

In variational quantum algorithms, feature map circuits are recommended such as *PauliFeatureMap*, *ZFeatureMap*, and *ZZFeatureMap* [16]. At first, as shown in Fig. 3(a), *ZFeatureMap* is the first order Pauli Z-evolution circuit and a sub-class of *PauliFeatureMap* where the Pauli strings are fixed as $['Z']$. The *ZFeatureMap* encodes classical datasets $x^{(m)}$ into a quantum state as follows

$$U_{\text{ZFeatureMap}}(x^{(m)}) = \prod_{i=1}^N \left(R_Z \left(2x_i^{(m)} \right) H_i \right), \quad (10)$$

where $R_Z(2x_i^{(m)})$ denotes a Z -axis rotation gate by an angle $2x_i$. H denotes the operation of the Hadamard gate.

As shown in Fig. 3(b), *ZZFeatureMap* is the second order Pauli Z-evolution circuit and a sub-class of *PauliFeatureMap*

where the Pauli strings are fixed as $[ZZZ]$. The $ZZFeatureMap$ encodes classical datasets $x^{(m)}$ into a quantum state as follows

$$U_{ZZFeatureMap}(x^{(m)}) = \prod_{i=1}^N R_Z \left(2x_i^{(m)} \right) \circ \prod_{i < j} \mathbf{CR}_Z \left(2x_i^{(m)} x_j^{(m)} \right) \mathbf{H}_i, \quad (11)$$

where $\mathbf{CR}_Z \left(x_i^{(m)} x_j^{(m)} \right)$ denotes a controlled Z gate (CZ) that is combined with CX and Z gate.

2) *Quantum circuit*: An ansatz is a parameterized quantum circuit employed to derive a measurable state from an input-encoded initial state, subsequently defining the classifier's output. By adjusting the weight parameters, it approximates solutions to specific problems. This forms a hypothesis space for optimization, where the weight parameters are iteratively refined to optimize a given objective function. Using an ansatz $U_Q(\theta)$, a state $|\psi(\theta)\rangle = U_Q(\theta)|0\rangle$ is used for measurement.

In variational quantum algorithms, ansatz circuits are given such as *RealAmplitudes*, *EfficientSU2*, *TwoLocal* [18]. *EfficientSU2* is the hardware efficient 2-local circuit, which consists of layers of single-qubit operations spanned by SU(2) and CX entanglement. SU(2) stands for special unitary group of degree 2, its elements are 2×2 unitary matrices with determinant 1, such as the Pauli rotation gates. This research presents a modification of the *EfficientSU2* algorithm by replacing the CX entanglement gates with CZ gates. The revised ansatz can be expressed as a quantum state in the following manner.

$$U_Q(\theta) = \left(\prod_{i=1}^N R_Z(\theta_i) R_Y(\theta_i) \right) \circ \prod_{p=1}^{r_{rep}} \left\{ \left(\prod_{m=1}^M \mathbf{CZ} \left(q_M^{(p)} | q_{M-1}^{(p)} \right) \otimes \dots \otimes \mathbf{CZ} \left(q_2^{(p)} | q_1^{(p)} \right) \right) \left(\prod_{i=1}^N R_Z(\theta_{i,p}) R_Y(\theta_{i,p}) \right) \right\}, \quad (12)$$

where $R_Y(\theta_i)$ denotes a Y-axis rotation gate.

3) *Measurement*: Measurement refers to the process of extracting a classical N -bit from N quantum states. The qubits are converted into a definite classical bit (0 or 1) based on the probability of the quantum state. Therefore, measurement yields a classical outcome depending on the overlap with the Pauli-Z eigenstates as follows.

$$|\psi(\alpha_i; \theta)\rangle \xrightarrow{\text{measurement}} \begin{cases} 0 \text{ (outcome + 1)} \\ \text{with } p_0 = |\langle \psi(\alpha_i; \theta) | 0 \rangle|^2, \\ 1 \text{ (outcome - 1)} \\ \text{with } p_1 = |\langle \psi(\alpha_i; \theta) | 1 \rangle|^2. \end{cases} \quad (13)$$

4) *Optimization*: QNN typically operates in a quantum-classical hybrid framework. The classical part includes evaluating the cost/loss function and optimizing the parameters.

This study examines the cross entropy loss function used in multiclass classification, with the function represented as

$$\mathcal{L}_{CE}(\theta) = -\frac{1}{M} \sum_{i=1}^M \sum_{j=1}^C y_{i,j} \log(f(\hat{y}_{i,j})), \quad (14)$$

where M is the number of samples, C is the number of classes, $y_{i,j}$ represents the binary truth label of 0 or 1, and $f(\hat{y}_{i,j})$ denotes the predicted output probability.

For QNN, classical optimizers are used, such as constrained optimization by linear approximation (COBYLA) and sequential least squares programming (SLSQP) [19].

COBYLA is a gradient-free optimization algorithm that uses a linear approximation of the function in the vicinity of the current point to select the next evaluation point. Two crucial parameters within COBYLA are rhobeg and maxiter. The rhobeg defines the initial size of the trust region surrounding the starting point, and the maxiter sets the limit on the number of iterations the algorithm can execute before stopping.

SLSQP is a sequential least squares programming algorithm that uses a black-box function. The objective function and the constraints are differentiable twice continuously. Three crucial parameters within SLSQP are ftol, eps, and maxiter. The ftol defines the precision goal for the value in the stopping criterion and the eps defines step size used for the numerical approximation of the Jacobian. The maxiter functions similarly to the COBYLA parameter. For SLSQP, the gradient is estimated at each iteration t , and then the parameter update θ can be expressed as follows:

$$\theta_{t+1} = \theta_t - \gamma \nabla \mathcal{L}_{CE}(\theta_t), \quad (15)$$

where γ is the learning rate and set to $\gamma = 0.01$ in this study.

C. Complexity Analysis

Classical NN exhibit a complexity of $\mathcal{O}(N_{\text{layer}}(N_{\text{neuron}})^2)$, while QNN show a reduced complexity of $\mathcal{O}(N_{\text{layer}}N_{\text{neuron}})$, where N_{layer} and N_{neuron} represents the number of layers and neurons [12].

The complexity of the QNN framework can be represented as the sum of the complexity of both the input encoding (enc) and the ansatz (Q) circuits, which is expressed by

$$\mathcal{O}_{\text{tot}} = \mathcal{O}_{\text{enc,gate}} + \mathcal{O}_{\text{enc,entg}} + \mathcal{O}_{\text{Q,gate}} + \mathcal{O}_{\text{Q,entg}}, \quad (16)$$

where each circuit consists of quantum gate operations (gate) followed by an entanglement layer operation (entg). The complexity of each quantum gate, including R_Y and R_Z , is denoted by $\mathcal{O}(1)$ [12]. The total complexity associated with a quantum gate is represented as $\mathcal{O}(N_g)$, where N_g denotes the total number of gates. Circular entanglement requires $\mathcal{O}\left(\frac{r(r-1)}{2}\right)$ operations for r qubits, as each entanglement layer involves gate operations between qubit pairs [20].

By employing the designated input encoding and ansatz detailed in [16], [18], we evaluate the computational complexity associated with the QNN architecture. Input encoding termed $ZFeatureMap$ is not involved entanglement, resulting in a total complexity of $\mathcal{O}(r_{rep}r)$. Here, the total number of gates matches the number of gates, expressed as $N_g = r$ and r_{rep}

TABLE I
SIMULATION PARAMETERS, WHERE r , r_{rep} IS THE NUMBER OF QUBITS
AND REPEATED CIRCUITS.

Parameters	Values
QNN setup	
Simulator	IBM Qiskit [21]
Ansatz	Modified <i>EfficientSU2</i> [18]
Loss function	Cross entropy
Optimizer	COBYLA, SLSQP [19]
Samples, M	200 per class
Scenario	S1: BPSK+BPSK S2: BPSK+QPSK S3: QPSK+QPSK
Detectors $S[r, \{enc\}]$	ML: S1[2, ZZ], S2[3, ZZ], S3[4, ZZ] SIC: S1[1, Z], S2[3, {Z, ZZ}], S3[2, ZZ] RML: S1[2, {Z, Z}], S2[3, {Z, ZZ}], S3[4, {ZZ, ZZ}]
r_{rep}	2
NOMA setup	
K	2
p_1, p_2	(0.2, 0.8)

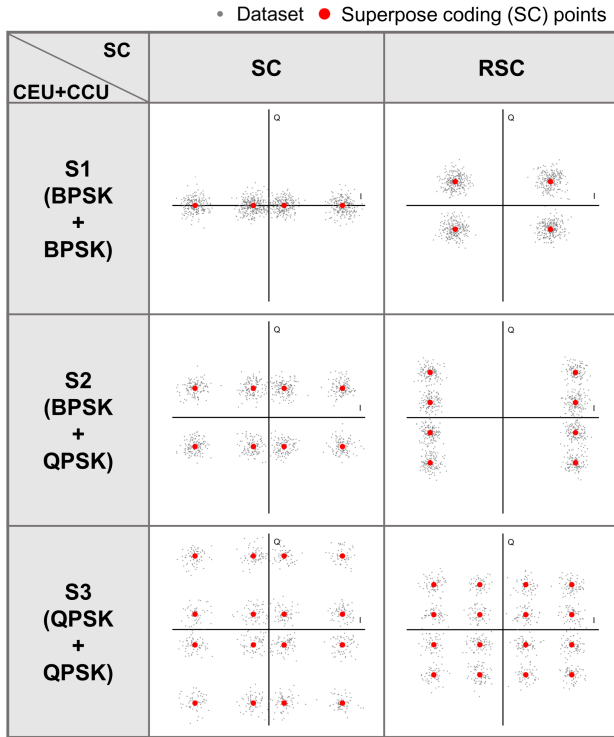


Fig. 4. Dataset of NOMA constellation where SNR=15 dB.

represents the number of repeated circuits. In contrast, *ZZFeatureMap* involves entanglement, resulting in a total complexity of $\mathcal{O}\left(r + r_{rep} \frac{r(r-1)}{2}\right) + \mathcal{O}(r_{rep}r(r-1))$. The total gate count, $N_g = r + r_{rep} \frac{r(r-1)}{2}$, and entanglement occur $r(r-1)$ times, with r_{rep} repetitions. The complexity of the modified *EfficientSU2* ansatz is $\mathcal{O}(2r(1 + r_{rep})) + \mathcal{O}(r_{rep}r(r-1))$.

IV. RESULT AND DISCUSSION

This section provides the used dataset and presents numerical results for the evaluation of three QNN-based NOMA

detectors (ML, SIC, RML), examining metrics such as loss, accuracy and testing across different signal-to-noise ratio (SNR) levels and power allocation coefficients. Quantum operations were executed on the IBM Quantum platform using IBM Qiskit [21]. Moreover, we provide a comparative analysis between DNN and QNN by examining training loss and accuracy metrics for the ML detector. The architecture and size of the DNN model are configured to mirror that of the model described in [22].

A. Dataset

A dataset was generated using MATLAB consisting of 200 samples per class for each SNR ranging from 0 to 30 dB in increments of 5. This study uses the classical input data derived from the received signal according to (3), assuming ideal channel estimation. Therefore, the dataset is constructed by adding additive white Gaussian noise (AWGN) to the SC constellation points of NOMA. Three NOMA scenarios, employing BPSK or QPSK modulation for each user, were evaluated using a QNN based NOMA detector. The constellation points for the three NOMA scenarios are illustrated in Fig. 4 for basic NOMA and rotated NOMA. A NOMA pair is formed by two users using the modulation (CEU+CCU). We examine three distinct NOMA scenarios : S1(BPSK+BPSK), S2(BPSK+QPSK), S3(QPSK+QPSK) as outlined in Table I.

To distribute the training and testing samples, the entire datasets was divided into 80 % for training and 20 % for testing, with the same subcategory distribution preserved in each class.

B. Evaluation of QNN based NOMA Detector

The QNN-based NOMA detector's performance is evaluated using conventional classifier evaluation metrics that include accuracy, precision, recall, and the F1 score.

$$\begin{aligned}
 Accuracy &= \frac{TP + TN}{TP + TN + FP + FN}, \\
 Precision &= \frac{TP}{TP + FP}, \\
 Recall &= \frac{TP}{TP + FN}, \\
 F_1Score &= 2 \times \frac{Precision \times Recall}{Precision + Recall},
 \end{aligned} \tag{17}$$

where TP , TN , FP , FN denote true positive, true negative, false positive, false negative, respectively.

C. Numerical Results

1) *Training loss*: In Fig. 5, the differences in training loss between QNN and DNN for an ML detector of the NOMA system are illustrated, where the SNR is fixed at 15 dB. It is observed that the QNN-based ML detector achieves convergence more rapidly during training compared to its DNN counterpart.

TABLE II
PERFORMANCE EVALUATION FOR VARIOUS DETECTORS WITH
SCENARIO 1.

Detector	Class	Performance evaluation		
		Precision	Recall	F1 score
ML	0	0.86	0.66	0.74
	1	1	1	1
	2	1	1	0.74
	3	0.74	0.90	0.81
SIC	CEU	0	1	1
		1	1	1
	CCU	0	0.99	0.99
		1	0.99	0.99
RML	CEU	0	1	1
		1	1	1
	CCU	0	0.98	0.99
		1	0.99	0.99

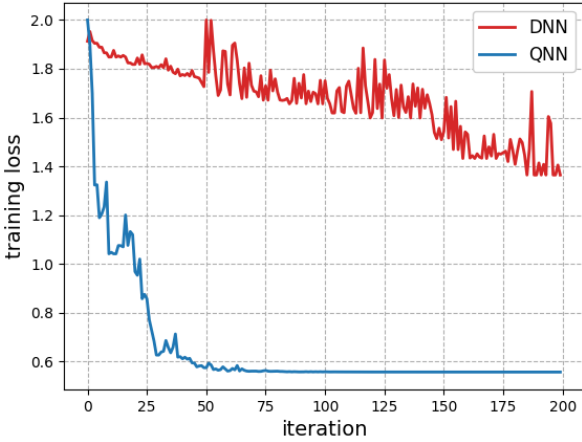


Fig. 5. Loss comparison between DNN and QNN using ML detector.

2) *Evaluation metrics*: Table II displays the performance metrics of the three detectors, considering the NOMA pair configuration S1 (BPSK + BPSK). These performance figures facilitate the comparison between the predicted and actual classes, as outlined in Section IV-B. The confusion matrix and the number of qubits for three NOMA detectors, corresponding to scenarios S1 and S2, are depicted in Fig. 6. S3 is excluded from the figure; it shares the same number of QNN frameworks as S1 for training. However, the class configuration is modified to 16 for ML, 4 for SIC, and 4 for each RML.

3) *Accuracy vs. SNR*: Fig. 7 illustrates the accuracy for three different NOMA scenarios, comparing different NOMA detectors against varying SNR levels. As the number of classes increases (scenario from (a) to (c)), all methods exhibit degraded performance and encounter difficulties in achieving high accuracy, particularly at lower SNR levels. The results show that the ML detector underperforms across all scenarios, whereas SIC and RML exhibit comparable performance. Furthermore, the ML detector employing DNN exhibits marginally better accuracy than that utilizing QNN.

4) *Test with different SNR*: Fig. 8 illustrates the comparison of accuracy under varying SNR levels between the training and testing datasets, with training in SNR of 15 dB, while testing in SNR of 10 and 20 dB. Compared to Figs. 7 and 9, although

TABLE III
COMPARISON OF OPTIMIZATION ACCURACY: COBYLA VS. SLSQP, WITH
SUPERIOR RESULTS HIGHLIGHTED IN BOLD.

Detector	Scenario	Optimization	
		COBYLA	SLSQP
ML	S1	0.637	0.630
	S2	0.530	0.590
	S3	0.223	0.240
SIC	S1	0.940	0.915
	S2	0.872	0.890
	S3	0.843	0.847
RML	S1	0.992	0.990
	S2	0.775	0.785
	S3	0.670	0.677

TABLE IV
COMPLEXITY COMPARISON WHEN $r_{rep} = 2$.

Detector	S1	S2	S3
ML	$\mathcal{O}(22)$	$\mathcal{O}(43)$	$\mathcal{O}(70)$
SIC	$\mathcal{O}(8)$	$\mathcal{O}(30)$	$\mathcal{O}(22)$
RML	$\mathcal{O}(16)$	$\mathcal{O}(30)$	$\mathcal{O}(44)$

training at each specific SNR level provides optimal results, it is feasible to apply training exclusively at an SNR of 15 dB. The resulting weights can be applied efficiently to adjacent SNR levels.

5) *Test with different PA coefficient*: Fig. 9 shows the comparison of accuracy under varying PA coefficient of CCU p_1 between the training and testing datasets, with training in $p_1 = 0.2$, while testing in $p_1 = 0.1$ and 0.3 , where SNR is fixed at 15 dB. Relative to Fig. 9, altering the PA coefficient between training and testing worsens ML and SIC performance due to significant alterations in basic SC constellation points. For scenarios (a) and (c), $p_1 = 0.2$ leads to equidistant symbol placement, leading to performance degradation for testing. However, scenario (b) lacks this uniformity, causing reduced accuracy in training and testing. Meanwhile, RML remains unaffected by coefficient variations, as RSC ensures optimal uniform positioning, mirroring the performance trend in Fig. 8.

6) *Optimization comparison*: Table III presents a comparative analysis of the accuracy of COBYLA and SLSQP optimization in three detectors and NOMA scenarios. It can be observed that SLSQP has performed slightly better than COBYLA as the modulation order for the NOMA pair increases.

7) *Complexity*: Table IV illustrates the complexity evaluation of three NOMA detectors based on 16, employing the modified *EfficientSU2* ansatz and the encoding configuration according to Table. I, where $r_{rep} = 2$. For example, when S1 (BPSK + BPSK), the ML detector uses 2 qubits and one ZZ gate, then complexity is $\mathcal{O}_{tot} = \mathcal{O}(4) + \mathcal{O}(4) + \mathcal{O}(12) + \mathcal{O}(2) = \mathcal{O}(22)$. In all scenarios, the complexity of the ML detector surpasses that of other detectors. Furthermore, SIC demonstrates lower complexity than RML, except when each user employs a different modulation order.

V. CONCLUSION

This study has presented a performance evaluation of a QNN-based NOMA detector such as multiclass classification.

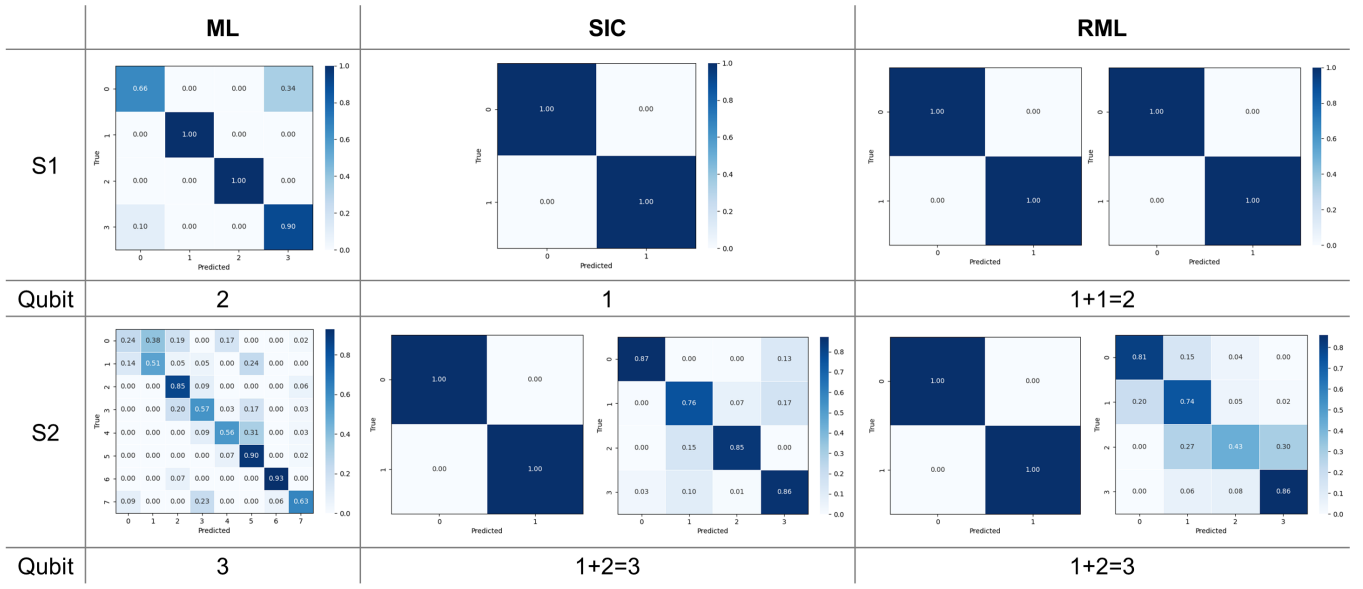


Fig. 6. Confusion matrix and the number of qubits corresponding to three NOMA detectors for S1 and S2.

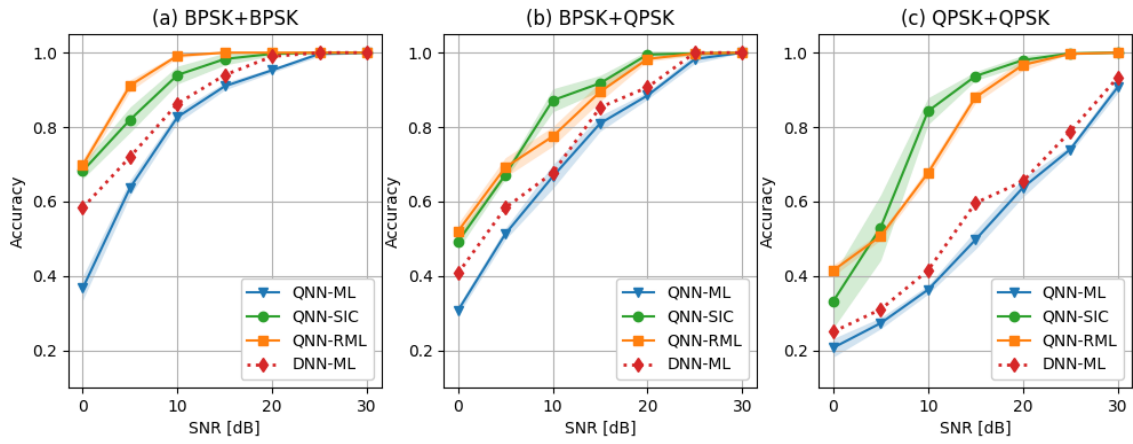


Fig. 7. Accuracy with three NOMA scenarios accuracy comparing different NOMA detectors against varying SNR levels.

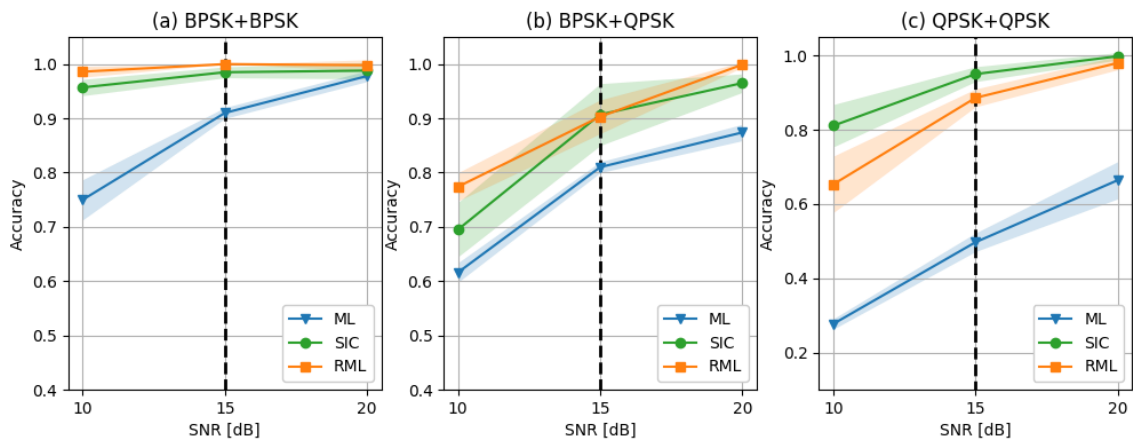


Fig. 8. Accuracy comparison with different SNR : training $SNR = 15$ dB and testing $SNR = 10, 20$ dB.

The analysis encompassed two SCs and three detector methods in a two-user downlink NOMA scenario. A QNN framework

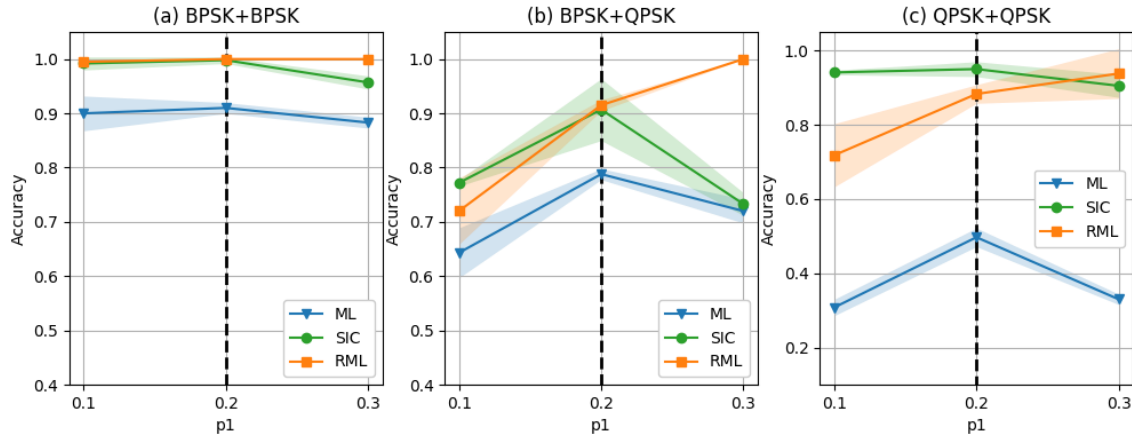


Fig. 9. Accuracy comparison with different power allocation coefficient: training $p_1 = 0.2$ and testing $p_1 = 0.1, 0.3$.

was configured for all three detectors, and a comparative analysis was conducted in terms of accuracy under various conditions of the SNR and power coefficient, considering NOMA-specific characteristics. Compared to DNN, QNN-based models showed quicker convergence in training loss, but exhibited marginally lower accuracy after validation loss stabilized. Furthermore, the computational complexity of each detector was analyzed in terms of quantum gate operations within the proposed QNN framework. It was found that the SIC and RML detectors, despite requiring multiple QNN structures, exhibited lower complexity than the ML detector. Notably, when both users employ the same modulation order, the SIC method allows one QNN training phase to be omitted, leading to further complexity reduction.

Future research will integrate resource allocation [12] into the NOMA detector, while examining the impact of imperfect SIC in practical, including such as fading channels, inter-user interference, and dynamic environments. For the QNN architecture, our aim will be to explore input encoding techniques that minimize qubit consumption while maintaining similar effectiveness.

REFERENCES

- [1] S. Dang, O. Amin, B. Shihada, and M.-S. Alouini, "What should 6G be?" *Nature Electron.*, vol. 3, no. 1, pp. 20–29, 2020.
- [2] C. Li, W. Guo, S. C. Sun, S. Al-Rubaye, and A. Tsourdos, "Trustworthy deep learning in 6G-enabled mass autonomy: From concept to quality-of-trust key performance indicators," *IEEE Veh. Technol. Mag.*, vol. 15, no. 4, pp. 112–121, 2020.
- [3] D. Sharma, V. Tilwari, and S. Pack, "An overview for designing 6G networks: Technologies, spectrum management, enhanced air interface and AI/ML optimization," *IEEE Internet Things J.*, vol. 12, no. 6, 2024.
- [4] A. Abbas *et al.*, "The power of quantum neural networks," *Nature Comput. Sci.*, vol. 1, no. 6, pp. 403–409, 2021.
- [5] N. H. Nguyen, E. C. Behrman, M. A. Moustafa, and J. E. Steck, "Benchmarking neural networks for quantum computations," *IEEE Trans. Neural Net. Learn. Syst.*, vol. 31, no. 7, pp. 2522–2531, 2019.
- [6] Y. Li, R.-G. Zhou, R. Xu, J. Luo, and W. Hu, "A quantum deep convolutional neural network for image recognition," *Quantum Sci. Technol.*, vol. 5, no. 4, p. 044003, 2020.
- [7] C. Wang and A. Rahman, "Quantum-enabled 6G wireless networks: Opportunities and challenges," *IEEE Wireless Commun.*, vol. 29, no. 1, pp. 58–69, 2022.
- [8] B. Narottama, Z. Mohamed, and S. Aïssa, "Quantum machine learning for next-G wireless communications: Fundamentals and the path ahead," *IEEE Open J. Commun. Soc.*, vol. 4, pp. 2204–2224, 2023.
- [9] N. Ye, J. An, and J. Yu, "Deep-learning-enhanced NOMA transceiver design for massive MTC: Challenges, state of the art, and future directions," *IEEE Wireless Commun.*, vol. 28, no. 4, pp. 66–73, 2021.
- [10] S. R. Islam, M. Zeng, O. A. Dobre, and K.-S. Kwak, "Resource allocation for downlink NOMA systems: Key techniques and open issues," *IEEE Wireless Commun.*, vol. 25, no. 2, pp. 40–47, 2018.
- [11] B. Narottama, T. Jamaluddin, and S. Y. Shin, "Quantum neural network with parallel training for wireless resource optimization," *IEEE Trans. Mobile Comput.*, vol. 23, no. 5, 2023.
- [12] B. Narottama and S. Y. Shin, "Quantum neural networks for resource allocation in wireless communications," *IEEE Trans. Wireless Commun.*, vol. 21, no. 2, pp. 1103–1116, 2021.
- [13] A. Barenco *et al.*, "Elementary gates for quantum computation," *Physical review A*, vol. 52, no. 5, p. 3457, 1995.
- [14] A. Chauhan and A. Jaiswal, "Non-orthogonal multiple access: A constellation domain multiplexing approach," in *IEEE PIMRC*, pp. 1–6, 2020.
- [15] H. Y. Lee and S. Y. Shin, "A novel user grouping in phase rotation based downlink NOMA," *IEEE Access*, vol. 10, pp. 27211–27222, 2022.
- [16] V. Havlíček *et al.*, "Supervised learning with quantum-enhanced feature spaces," *Nature*, vol. 567, no. 7747, pp. 209–212, 2019.
- [17] R. LaRose and B. Coyle, "Robust data encodings for quantum classifiers," *Physical Review A*, vol. 102, no. 3, p. 032420, 2020.
- [18] A. Javadi-Abhari *et al.*, "Quantum computing with Qiskit," *arXiv preprint arXiv:2405.08810* 2024.
- [19] P. Virtanen *et al.*, "Fundamental algorithms for scientific computing in python and SciPy 1.0 contributors," *Nat. Methods*, vol. 17, pp. 261–272, 2020.
- [20] T. Nandi, A. Baghel, A. K. Pathak, and V. Bhatia, "Hybrid quantum machine learning model for power allocation in NOMA," in *IEEE CICT*, 2024.
- [21] Qiskit contributors, "Qiskit: An open-source framework for quantum computing," 2023.
- [22] J. Thompson *et al.*, "Deep learning for signal detection in non-orthogonal multiple access wireless systems," in *UCET*, 2019.



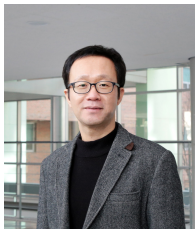
input multiple-output (MIMO) antenna, index modulation (IM), and orbital angular momentum (OAM).

Hye Yeong Lee received the B.S. degree in Electrical Engineering and the M.S. and Ph.D. degrees in IT Convergence Engineering from Kumoh National Institute of Technology (KIT), South Korea, in 2016, 2018, and 2022, respectively. She is currently working as a Postdoctoral Fellow and a Researcher at Wireless and Emerging Network System (WENS) Lab, SUMMIT Research Center, KIT. Her research interests include 6G wireless communications and networks, signal processing, non-orthogonal multiple access (NOMA), multiple-



future radio access (FRA) for next generation networks, non-orthogonal multiple access (NOMA), orbital angular momentum (OAM), MIMO, DSP, etc.

Man Hee Lee received his B.S. in Electrical Engineering and M.S. and Ph.D. in Department of IT Convergence Engineering from Kumoh National Institute of Technology (KIT) Gumi, South Korea, in 2016, 2018, and 2024. From 2018 to 2020, he worked as DSP/FW Engineer at the company. Currently, he is working as Postdoctoral Fellow at Wireless and Emerging Network System (WENS) Lab., Department of IT Convergence Engineering, Kumoh National Institute of Technology (KIT), Gumi, South Korea. His main research areas are



interests include wireless LAN, WPAN, WBAN, wireless mesh networks, sensor networks, coexistence among wireless networks, industrial and military networks, cognitive radio networks, and next-generation mobile wireless broadband networks.

Soo Young Shin (Senior Member, IEEE) received the B.S., M.S., and Ph.D. degrees in Electrical Engineering and Computer Science from Seoul National University, South Korea, in 1999, 2001, and 2006, respectively. He was a Visiting Scholar with the FUN Laboratory, University of Washington, USA, from July 2006 to June 2007. After three years working at the WiMAX Design Laboratory, Samsung Electronics, he has been an Associate Professor with the School of Electronics, Kumoh National Institute of Technology, since September 2010. His research